Spatial Structure of Far Ultraviolet Martian Dayglow Observed by EMM-EMUS

S. L. England[1], S. Jain[2], J. Deighan[2], M. Chaffin[2], G. Holsclaw[2], J. S. Evans[3], J. Correira[3], M. O. Fillingim[4], R. L. Lillis[4], H. Al Matroushi[5], F. Lootah[5], and H. Al Mazmi[6]

[1] Aerospace and Ocean Engineering, Virginia Polytechnic Institute and State University, Blacksburg, Virginia, United States

[2] Laboratory for Atmospheric and Space Physics, University of Colorado, Boulder, United States

[3] Computational Physics, Inc., Springfield, Virginia, United States

[4] Space Sciences Lab, University of California, Berkeley, California, United States

[5] Mohammed Bin Rashid Space Centre, Dubai, United Arab Emirates

[6] UAE Space Agency, Abu Dhabi, United Arab Emirates

Corresponding author: Scott L. England (englands@vt.edu), Orcid: 0000-0001-5336-0040

Key points

1. Variations in the ultraviolet dayglow from the Martian thermosphere with local time and emission viewing angle are characterized

2. Asymmetry in the airglow between dawn and dusk varies by emission from +15.4% to -12.3% in response to transport and temperature
3. Patches of significant airglow brightness increase are observed that appear to result from changes in composition and photoelectron flux

Abstract

Mars' ultraviolet airglow has been used to study its upper atmosphere for over four decades. Identifying variations in emission features has provided information on composition, density and temperature. The Emirates Mars Ultraviolet Spectrometer onboard the Emirates Mars Mission observes Mars' airglow at Far and Extreme UV wavelengths. Variations in disk emission features are studied, with a focus on O I 1304 Å, CO Fourth Positive Group and C I 1561 Å. All show variations with local time and emission angle as expected. Dawn-dusk asymmetry observed is attributed to local time differences in advection. Variations in the brightness of several dayglow features, including 1304 Å, with irregular shapes are noted in around 25% of the disk images. These display some local time and hemispheric asymmetry in their occurrence rates. Examination of their spatial structure, occurrence, and spectra suggests these are associated with variations in composition and photoelectron flux.

Plain Language Summary

Measurements of ultraviolet light coming from Mars' upper atmosphere has been used to measure its properties. From the color and brightness of the light, it is possible to identify both what chemical species are present in this region, their temperature and other information. The

Emirates Mars Ultraviolet Spectrometer onboard the Emirates Mars Mission makes observations of this ultraviolet light in wavelength regions described as far and extreme ultraviolet. This study looks at emissions of far ultraviolet light that correspond to oxygen atoms, carbon monoxide and carbon dioxide molecules. The circulation of gases in the upper atmosphere results in a difference in the brightness of these emissions between dawn and dusk. This study also introduces observations of irregularly shaped bright patches in these emissions. The shape, location, and spectra of these suggest they are the result of changes in the chemical composition of the upper atmosphere.

1 Introduction

Observations of ultraviolet airglow provide information about the composition, energetics and dynamics of planetary atmospheres and ionospheres (e.g., Hendrix *et al*., 2014). The first such observations of Mars were taken by the Mariner 6, 7 and 9 spacecraft (e.g., Barth *et al*., 1969; Stewart, 1972). These covered the Far and Mid ultraviolet (FUV, MUV) from ~1100 to 4300 Å and revealed airglow features associated with H (Lyman alpha), O (1304 and 1356 Å), C (1561 and 1657 Å), CO (Fourth Positive Group and Cameron bands) and CO_2^+ (Ultraviolet Double and Fox-Duffendack-Barker bands). Subsequently, the UV airglow of Mars has been observed by spacecraft orbiting Mars including Mars 2 and 3 (e.g., Dementyeva *et al*., 1972), Mars Express (e.g., Bertaux *et al*., 2006), Mars Atmosphere and Volatile EvolutioN (MAVEN) (e.g., McClintock *et al*., 2014), and ExoMARS Trace Gas Orbiter (e.g., López-Valverde *et al*., 2018). In addition to these, observations from Earth orbit from the Extreme UV Explorer (e.g., Krasnopolsky, 2002), Hubble Space Telescope (e.g., Bhattacharyya *et al*., 2017) and the Hopkins University Telescope (HUT; e.g., Feldman *et al*., 2000). Collectively, these have provided insight into Martian upper atmosphere (e.g., Jain *et al*., 2015; Evans *et al*., 2015), and ozone, clouds and dust at lower altitudes (e.g., Stevens *et al*., 2017).

Observations of the Martian airglow can be grouped into two broad categories: those made of the limb that can provide altitude resolved measurements; and those made of the disk of the planet, which provide no altitude resolution but can offer more spatial coverage per observation. At Mars, disk observations of EUV and FUV airglow provide information on the upper atmosphere, owing to strong CO_2 absorption below.

The Emirates Mars Mission (EMM; Amiri *et al*., 2021) was launched in July 2020, reaching Mars in February 2021. From its high-altitude, 54.5-hour orbit, EMM is focused on studying the Martian atmosphere, its connection to the exosphere and atmospheric escape (Al-Matroushi *et al*., 2021). The Emirates Mars Ultraviolet Spectrometer (EMUS) is a one-dimensional imaging ultraviolet spectrometer, designed to observe the upper atmosphere and exosphere (Holsclaw *et al*., 2021). EMUS began taking regular science data in June 2021. These data consist of observation sequences that build up 2D spectral images. Of the four prime observing sequences, OS1 and OS2 are focused on the upper atmosphere (further details are given by Holsclaw *et al*., 2021).

This work presents the EMM EMUS disk observations of the Martian dayglow. Section 2 introduces these data, with a focus on three emission features. Section 3.1 shows the overall pattern of these features, their variation with local time and viewing angle. Section 3.2 highlights how the observations sometimes deviate significantly from these overall patterns. The occurrence and their nature of these are investigated.

2 Data

EMUS observes the Martian airglow from 830 – 1800 Å. Details of the instrument design and performance are described by Holsclaw *et al*., (2021). The instantaneous field of view (FOV) is a narrow slit, 10.75° in the imaging direction. The disk observations used here are made from EMM's high altitude (periapsis 19,970 km, apoapsis 42,650 km), 25° inclination orbit. An image of the disk is built-up by sweeping the FOV perpendicular to the imaging direction. This is done in two operating modes, OS1 and OS2. OS1 scans take 8.9 – 17.4 minutes (apoapsis – periapsis), utilize a 13 Å resolution slit, and 2 scans provide full coverage. OS2 take 11.2 – 21.8 minutes, utilize a 18 Å resolution slit, and 3 scans provide full coverage. Both scan durations are short compared to both the orbital period (54.5 hours) and Mars' rotation, so can be treated as snapshots. Both have high enough spectral resolution to identify the dayglow features examined here, so are used interchangeably hereafter.

This study uses the Level 2B data. The process of producing Level 2B data is described in detail in Holsclaw *et al*., (2021). Briefly, counts are converted to calibrated spectral images by calibrating for the radiometric sensitivity, detector dead time, wavelength distortion, binning data into science pixels (0.08 x 0.36°) and convolving the observed spectra with the instrument's line-spread function. The brightness of individual airglow features are identified using a multiple linear regression scheme, similar to that employed for MAVEN-IUVS (Jain *et al*., 2015; Stevens *et al*., 2015).

Three airglow features are highlighted in this study, each selected to demonstrate the range of behavior observed. These are: 1304 Å from O 3s → 3p (e.g., Barth *et al*., 1971; O1304 hereafter), the CO (14,0) band of the Fourth Positive Group ($A^1\Pi \rightarrow X^1\Sigma^+$; CO4PG hereafter), and 1561 Å from C 3d → 3p (e.g., Barth *et al*., 1971; C1561 hereafter). O1304 comes from resonant scattering of sunlight (Strickland *et al.*, 1972, 1973; Stewart *et al.*, 1992), electron impact on O, CO, and CO_2 (Ajello, 1971a; Ajello, 1971b; Zipf and Erdman, 1985), and photodissociative excitation of CO and CO_2 (Gentieu and Mentall, 1972; Wu and Judge, 1979). The photodissociation sources are negligible compared to resonant scattering and electron impact on O (Simon et al., 2009; Chaufray *et al.*, 2009). There is also blending with CO 4PG at 1304 Å, however the contribution is weak relative to dominant sources. The 4PG emission at 1356 Å is a blend of the O I 1356 Å doublet, the CO 4PG (14,4) band excited by solar Lyman alpha photons, and a weak contribution from the N_2 LBH (3,0) band, where the relative contributions are dictated by the local O, CO, and N_2 mixing ratios, respectively (Kassal, 1975, 1976; Durrance, 1981). Based on full disk observations of Mars using HUT, Feldman *et al*. (2000) concluded that most of the observed emission at 1356 Å is due to CO. The C1561 emission's primary excitation mechanism is photoelectron dissociative excitation of CO_2 at lower altitude, with a ~10% contribution from resonant scattering by C to the total column brightness (Lo *et al.*, 2022).

Figure 1 shows an example of the three airglow features for an example OS1. The solar zenith angles (SZA) are computed at 130 km altitude for all lines of site that intersect this surface. In each panel, the vertical direction corresponds to the 10.75° instantaneous FOV. All emissions show a general increase in brightness with decreasing SZA, dropping significantly at night. Additionally, all show an increase in brightness approaching the dayside limb, corresponding to high zenith emission angles (EMA). The horizontal banding visible in O1304 results from imperfections in the instrument flatfield along the imaging direction.

The following section explores the overall variation in airglow brightness with both EMA and local time. For this, a sequence of observations covering a wide parameter space are required. Selecting the OS1 and OS2 observations from June 11 – September 15, 2021 (solar longitude, L_s = 57° – 99°) provides sufficient coverage, while restricting seasonal and solar Extreme UV (EUV) changes as much as possible. Examining the MAVEN EUVM data for this time-period (Eparvier *et al.*, 2015) reveals that the solar EUV was nearly constant, with higher flux on July 13 and 15. Excluding the data take on these days effectively removes changes in solar EUV hereafter.

3 Method and Results

3.1 Dayglow Variations with Local Time and Emission Angle

To investigate the variation in the dayglow with LT and EMA, all OS1 and OS2 data described in Section 2 are used. As the L_s range is close to northern summer solstice, only data from ±5° latitude are included, leaving only variations in LT and EMA. All data are then binned into 1-hour by 10° bins for EMA ≤80° (avoiding the limb). Figure 2, panels a – c show the average (median) brightness of the three airglow features as functions of LT and EMA. The general variation is as expected, with the brightest airglow in all three emissions seen near local noon, and at higher EMA (corresponding to longer viewing path lengths through the airglow layer). Figure 2, panels d and e show this in more detail, where panel d shows the variation with EMA in all three emissions at 12 – 13 hours LT and panel e shows the variation with LT at 20 – 30° EMA. Both the median and one standard deviation ranges (resulting from both geophysical variations and measurement uncertainty) are shown. The variation with EMA shows an increase in all three emissions, but the relative increase for C1561 is notably larger than for the other two.

The variation with LT is similar for all three, with some morning – afternoon asymmetry visible. To investigate the morning-afternoon asymmetry in more detail, data close to dawn and dusk are selected. Here 7 – 8 LT is used to represent dawn and 16 – 17 LT for dusk to avoid the extremely low brightness at the terminator, especially in the C1561 emission. The dawn-dusk asymmetry is shown in Figure 2, panel f. Both the O1304 and CO4PG emissions show similar behavior, with dawn being ~10 – 20 % brighter than dusk at all EMA. The C1561 emission shows a distinctly different behavior, showing generally the opposite trend at most EMA, except for the very lowest. The positive asymmetry in C1561 in the 10 – 20 EMA bin should perhaps be viewed with caution as the dawn 0-10° EMA bin contains one tenth the number samples than any other, and the largest uncertainty of any point. Excluding this bin, the average asymmetry for O1304 is 13.5±3.1%, for CO4PG is 15.4±7.6%, and for C1561 is -12.3±6.1%.

3.2 Irregularly shaped Dayglow Variations

While the previous section showed the average variations in the dayglow with EMA and LT, this section focuses on notable departures from this behavior, where the variation in the brightness of the dayglow cannot be explained by geometric effects such as LT, SZA and EMA. Perhaps the most clearly visible of these are large (10s of degrees on the disk) regions where some of the airglow features are significantly brighter than expected, which occur in some of the disk scans. These are demonstrated clearly by contrasting the behavior of the O1304 and C1561 emissions. Figure 3 shows several examples of this. The left column shows an example from June 18, 2021, and the central column shows an example from approximately 5 hours later. The irregularly shaped bright features in O1304 are evident in both, with shapes and locations that do not follow either EMA or SZA. No similar features are evident in C1561. For a closer examination of the spectral differences between regions exhibiting this brightening in some airglow features, the right column of Figure 3 shows an example from July 22, 2021. In this example, the geometry of the observation provides the opportunity to sample two regions of the disk with almost identical SZA and EMA, one inside the bright region of O1304 and one outside (identified by the star and cross symbols). Panels f and I show the spectra averaged over 9 points around these two locations (to provide sufficient signal in the dimmer features). It can be seen from panel f that the brightness of O1304 is 40 % higher inside this region than the comparable location outside, which is well beyond the variation expected from the patterns shown in Figure 2, instrument noise etc. Panel i shows that these variations are strongly dependent on wavelength of the airglow, with some showing large increases such as the blended feature at 1356 Å and the CO Hopfield-Birge (B-X) (0,0) band near 1150 Å (which is expected to behave similarly to the CO 4PG as both are produced by thermal CO), while others see almost no change, including C1561 and the CI feature at 1657 Å, both of which are primary generated by electron impact dissociation of CO_2 (e.g., Lo, *et al*., 2022).

Examining a number of the irregularly shaped bright features in the O1304 emission, a wide range of shapes, sizes and locations are seen, and appear to occur somewhat sporadically over the dataset. To make progress in identifying potential sources of these features, the times and locations of where these features occur have been identified. As each feature has a different, amorphous shape, this identification has been done by eye. While this approach is potentially impact by human subjectivity, it offers perhaps a useful starting point before a more rigorous algorithm can be developed. For this study, all of the O1304 images during the three months considered were examined, and the presence of bright features occurring away from the limb that were not related to SZA, or EMA were noted, along with their approximate central latitude, longitude and LT. A complete list of these is given in the supplementary data.

Figure 4 shows the distribution of the irregularly shaped bright features identified. To interpret this distribution, it is important to consider the sampling distribution within the June – September, 2021 date range, which is shown in Figure 4, panels a and b as functions of latitude, longitude and LT. The distribution with latitude and longitude shows a greater concentration of datapoints at low latitude, with a drop-off beyond ±45° latitude. The distribution with latitude and LT highlights a morning (afternoon), northern (southern) hemisphere bias such that there are around three times as many samples in one hemisphere than the other near dawn and dusk at 30° latitude. Noting these trends, the distribution of the occurrences of irregularly shaped bright features in O1304 are shown in Figure 4, panels c and d. Panel d shows a clear hemispheric asymmetry in the occurrence rate of these features, with a higher occurrence rate in the northern hemisphere. No preferred longitude range is evident. Panel c shows a clear LT asymmetry, with a higher occurrence rate before local noon. Re-examining panel a, some amount of asymmetry is expected, as during the pre-noon hours there are more data available in the northern hemisphere than the southern hemisphere. Thus, if either the pre-noon or northern-hemisphere trends are real, the other may be expected. Looking at this in more detail, the asymmetry in the data availability at ±30° latitude at 9 LT is about a factor of 3. The asymmetry in the data availability at +30° latitude between 9 LT and 15 LT is about a factor of 2. The recorded asymmetry in the occurrence rate between north and south, and pre- and post-noon are both about a factor 7. This suggests that the observed asymmetry is not simply an artifact of the sampling distribution, although with a relatively small sample size it is not yet clear how strong the true asymmetry is.

4 Discussion and Conclusions

The equatorial disk brightness of three dayglow features (O 1304 Å, Lyman-Alpha pumped CO 4PG, and C 1561 Å) are examined for all data from June 11 – September 15, 2021 (solar longitude, L_s = 57° – 99°). Focusing on the median brightness, that are not significantly affected by the sporadic, irregularly shaped variations considered below, the following variations can be understood.

1) The brightness of all three dayglow features respond most directly to the angle to the sun (LT and/or SZA) and EMA. All three follow the same basic pattern of becoming brighter at lower SZA, and higher EMA, consistent with the changes in solar EUV input and ray path length through the emitting layer. The variations in CO4PG and O1304 are the most similar. The C1561 emission varies more strongly with EMA and varies in the opposite manner between near dawn and near dusk.
2) The change in brightness of the three emissions between low and high EMA are not all the same. For O1304, the variation between 5 – 75° degrees EMA is about a factor of 1.3, for CO4PG it is about a factor of 2 and for C1561 it is about a factor of 4. For optically thin emissions such as C1561, the increase with EMA is consistent with the varying ray path length through the emitting layer. For the optically thick O1304 and

CO4PG, further interpretation would require more detailed modeling of the airglow layer.

3) Focusing on the differences near dawn and dusk, O1304 and CO4PG display a similar degree of asymmetry, with dawn brighter than dusk at all EMA (averaging 13.5±3.1% and 15.4±7.6%, respectively). Assuming that the brightness of the O1304 and CO4PG emissions at a particular latitude, SZA and EMA is governed by the column ratios of O/CO_2 and CO/CO_2 in the Martin thermosphere respectively (as they are produced by resonant scattering of sunlight by O and CO, and absorbed by CO_2), the observed asymmetry can be attributed to the influence of advection on the composition of the thermosphere that is believed to produce asymmetries in He/CO_2 between dawn and dusk (e.g. Elrod, *et al*., 2017; Gupta, *et al*., 2021). Quantifying this compositional asymmetry for these optically thick emissions would require modeling that is beyond the scope of this paper. Across most EMA, C1561 displays the opposite dawn-dusk asymmetry (average of -12.3±6.1%.), which is consistent with it being primarily produced by photoelectron dissociative excitation of CO_2, which respond in the opposite sense to vertical advection.

Examining the whole disk images, around one quarter of the O1304 images display irregularly shaped variations in brightness that are not simply related to geometry. These patches of brighter airglow emission span 10s° across the disk, have amorphous shapes, and occur somewhat sporadically throughout the dataset.

1) The irregularly shaped bright features only appear in certain airglow features, and are perhaps clearest in O1304 as a result of its high signal to noise ratio (SNR), and the fact that the brighter spots are several 10s % brighter than otherwise comparable regions on the disk. The origin of these is unlikely to be instrumental noise, as they greatly exceed the SNR (the bright region in Figure 3c compared to the dimmer region has a SNR of 19 per pixel), are coherent across many adjacent pixels in each image, and show up at comparable strengths in several wavelengths. They are unlikely to be associated with true temporal changes in solar EUV flux, both as this is largely constant through the time-period analyzed and as any sudden change in solar EUV (e.g. from a flare) would create a signature that is aligned with the vertical direction in the images shown (which is not the case in Figure 3), and would not show up in successive images of the planet taken around 5 hours apart (Figure 3a, b). They are unlikely to be associated with precipitating electrons as they show no apparent correspondence to the crustal magnetic field regions (e.g., Connerney *et al*., 2001; Brain *et al*., 2003), and the magnitude of the signature seen (e.g., in O1304) is an order of magnitude larger than that seen in auroral signatures on the nightside (Lillis *et al*., this issue). Concluding that these are both real variations, and not caused by external factors that modulate the airglow production rate leaves real thermospheric variations as the most likely cause of these features. While a detailed analysis of the response of each emission to changing composition and photoelectron flux is beyond the scope of this paper, it is known that the production of photoelectrons at Mars is highly variable, and likely the result of changes in thermospheric composition (e.g., Lillis *et al*., 2021). Thus, one plausible

explanation for the irregularly shaped bright features in the airglow is changes in the thermospheric composition, perhaps amplified in terms of relative changes in the emission brightness via modulation of the photoelectron flux in the vicinity of the airglow peak. The variable response at different wavelengths is then plausibly the result of changes in the composition of the thermosphere.

2) Exploring the spatial and temporal distribution of the irregularly shaped features in O1304, the highest occurrence rates are seen in the northern hemisphere, before noon. Further data would be required to determine if this is always the case, or more simply reflects the limited L_s range examined here. No preferred longitude or latitude, beyond generally northern hemisphere, is apparent. The underlying cause of this remains unknown. Assuming that these features are associated with a real variation in thermospheric composition, interacting with varying photoelectron flux, further observations and modeling of the composition and resultant airglow will likely be required to fully understand the nature of these features.

Acknowledgements

Funding for development of the Emirates Mars mission was provided by the UAE government, and to co-authors outside of the UAE by MBRSC.

Open Research

The EMUS Level 2B data used in this study are available at the Emirate Mars Mission Science Data Center at https://sdc.emiratesmarsmission.ae/data/emus. This location is designated as the primary repository for all data products produced by the EMM team and is designated as long-term repository as required by the UAE Space Agency. MAVEN EUVM Level 2 data used are available at the PDS Planetary Plasma Interactions Node, https://pds-ppi.igpp.ucla.edu/mission/MAVEN/MAVEN/EUV. The locations of each point in Figure 4 are provided in Table S1.

References

Ajello, J. M. (1971a). Emission cross sections of CO by electron impact in the interval 1260–5000 Å. I. *The Journal of Chemical Physics*, *55*(7), 3158-3168.

Ajello, J. M. (1971b). Emission cross sections of CO2 by electron impact in the interval 1260–4500 Å. II. *The Journal of Chemical Physics*, *55*(7), 3169-3177.

Almatroushi, H., AlMazmi, H., AlMheiri, N. et al. Emirates Mars Mission Characterization of Mars Atmosphere Dynamics and Processes. Space Sci Rev 217, 89 (2021). https://doi.org/10.1007/s11214-021-00851-6

Amiri, H.E.S., Brain, D., Sharaf, O. et al. The Emirates Mars Mission. Space Sci Rev 218, 4 (2022). https://doi.org/10.1007/s11214-021-00868-x

Barth, C.A., W.G. Fastie, C.W. Hord, J.B. Pearce, K.K. Kelly, A.I. Stewart, G.E. Thomas, G.P. Anderson, O.F. Raper, Mariner 6 and 7: ultraviolet spectrum of Mars upper atmosphere. Science 165, 1004–1005 (1969)

Barth, C.A., Hord, C.W., Pearce, J.B., Kelly, K.K., Anderson, G.P., and Steward, A.I., Mariner 6 and 7 Ultraviolet Spectrometer Experiment: Upper atmosphere data. J. Geophys. Res. 76, 10 (1971). https://doi.org/10.1029/JA076i010p02213

Bhattacharyya, D., J.T. Clarke, J.Y. Chaufray, M. Mayyasi, J.L. Bertaux, M.S. Chaffin, N.M. Schneider, G.L. Villanueva, Seasonal changes in hydrogen escape from Mars through analysis of HST observations of the Martian exosphere near perihelion. J. Geophys. Res. Space Phys. 122(11), 11,756–11,764 (2017). https://doi.org/10.1002/2017JA024572

Bertaux, J.L., O. Korablev, S. Perrier, E.Q. merais, F. Montmessin, F. Leblanc, S. Lebonnois, P. Rannou, F. Lefére, F. Forget, A. Fedorova, E. Dimarellis, A. Reberac, D. Fonteyn, J.Y. Chaufray, S. Guibert, SPICAM on Mars Express: observing modes and overview of UV spectrometer data and scientific results. J. Geophys. Res. 111(E10), 10 (2006). https://doi.org/10.1029/2006JE002690

Brain, D. A., Bagenal, F., Acuña, M. H., & Connerney, J. E. P. (2003). Martian magnetic morphology: Contributions from the solar wind and crust, Journal of Geophysical Research, 108(A12), 1424. https://doi.org/10.1029/2002JA009482

Chaufray, J. Y., Leblanc, F., Quémerais, E., & Bertaux, J. L. (2009). Martian oxygen density at the exobase deduced from OI 130.4-nm observations by Spectroscopy for the Investigation of the Characteristics of the Atmosphere of Mars on Mars Express. *Journal of Geophysical Research: Planets*, *114*(E2).

Connerney, J. E. P., Acuña, M. H., Wasilewski, P. J., Kletetschka, G., Ness, N. F., Rème, H., ... Mitchell, D. L. (2001). The global magnetic field of Mars and implications for crustal evolution. Geophysical Research Letters, 28, 4015–4018. https://doi.org/10.1029/2001GL013619

Dementyeva, N.N., V.G. Kurt, A.S. Smirnov, L.G. Titarchuk, S.D. Chuvahin, Preliminary results of measurements of UV emissions scattered in the Martian upper atmosphere. Icarus 17, 475 (1972).

Durrance, S. T. (1981). The carbon monoxide fourth positive bands in the Venus dayglow 1. Synthetic spectra. *Journal of Geophysical Research: Space Physics*, *86*(A11), 9115-9124.

Elrod, M. K., S. Bougher, J. Bell, P. R. Mahaffy, M. Benna, S. Stone, R. Yelle, and B. Jakosky (2017), He bulge revealed: He and CO2 diurnal and seasonal variations in the upper atmosphere of Mars as detected by MAVEN NGIMS, J. Geophys. Res. Space Physics, 122, 2564–2573, doi:10.1002/2016JA023482.

Eparvier, F., Chamberlin, P. C., Woods, T. N., & Thiemann, E. M. B. (2015). The solar extreme ultraviolet monitor for MAVEN. Space Sciences Reviews, 195(1–4), 293–301. https://doi.org/10.1007/s11214-015-0195-2

Evans, J. S., Stevens, M. H., Lumpe, J. D., Schneider, N. M., Stewart, A. I. F., Deighan, J., et al. (2015). Retrieval of CO_2 and N_2 in the Martian thermosphere using dayglow observations by IUVS on MAVEN. *Geophysical Research Letters*, *42*, 9040–9049. https://doi.org/10.1002/2015GL065489.

Feldman, P.D., E.B. Burgh, S.T. Durrance, A.F. Davidsen, Far-ultraviolet spectroscopy of Venus and Mars at 4Å resolution with the Hopkins Ultraviolet Telescope on Astro-2. Astrophys. J. 538, 395–400 (2000). https://doi.org/10.1086/309125

Gentieu, E. P., & Mentall, J. E. (1973). Cross sections for production of the CO (A 1 Π− X 1 Σ) Fourth Positive band system and O (3 S) by photodissociation of CO_2. *The Journal of Chemical Physics*, *58*(11), 4803-4815.

Gupta, N., Rao, N. V., Bougher, S., & Elrod, M. K. (2021). Latitudinal and seasonal asymmetries of the helium bulge in the Martian upper atmosphere. Journal of Geophysical Research: Planets, 126, e2021JE006976. https:// doi.org/10.1029/2021JE006976

Hendrix, A.R., Nelson, R.M., and Domingue, D.L., (2014) Chapter 49 - The Solar System at Ultraviolet Wavelengths, Eds. Spohn, T., Breuer, D., and Johnson, T.V., Encyclopedia of the Solar System (Third Edition), Elsevier, Pages 1047-1071, ISBN 9780124158450, https://doi.org/10.1016/B978-0-12-415845-0.00049-9.

Holsclaw, G.M., Deighan, J., Almatroushi, H. et al. The Emirates Mars Ultraviolet Spectrometer (EMUS) for the EMM Mission. Space Sci Rev 217, 79 (2021). https://doi.org/10.1007/s11214-021-00854-3

Jain, S.K., A.I.F. Stewart, N.M. Schneider, J. Deighan, A. Stiepen, J.S. Evans, M.H. Stevens, M.S. Chaffin, M. Crismani, W.E. McClintock, J.T. Clarke, G.M. Holsclaw, D.Y. Lo, F. Lefèvre, F. Montmessin, E.M.B. Thiemann, F. Eparvier, B.M. Jakosky, The structure and variability of Mars upper atmosphere as seen in MAVEN/IUVS dayglow observations. Geophys. Res. Lett. 42, 9023–9030 (2015). https://doi.org/10. 1002/2015GL065419

Kassal, T., Resonant fluorescent scattering of solar radiation by the fourth positive band system of CO, Appl. Opt. 14, 1513-1515 (1975), doi:10.1364/AO.14.001513

Kassal, T. T. (1976), Scattering of solar Lyman alpha by the (14, 0) band of the fourth positive system of CO, J. Geophys. Res., 81(7), 1411– 1412, doi:10.1029/JA081i007p01411.

Krasnopolsky, V.A., Mars' upper atmosphere and ionosphere at low, medium, and high solar activities: implications for evolution of water. J. Geophys. Res. 107(E12), 5128 (2002). https://doi.org/10.1029/ 2001JE001809.

Lillis, R. J., Xu, S., Mitchell, D., Thiemann, E., Eparvier, F., Benna, M., & Elrod, M. (2021). Ionization efficiency in the dayside ionosphere of Mars: Structure and variability. Journal of Geophysical Research: Planets, 126, e2021JE006923. https://doi.org/10.1029/2021JE006923

Lillis, R. J., J., Deighan, M., Fillingim, S., Jain., M., Chaffin, G., Holsclaw, H., Al. Matroushi, F. Lootah, (This issue), First Synoptic Images of FUV Discrete Aurora at Mars by EMM EMUS

Lo, D.Y., Yelle, R.V., Deighan, J.I., Jain, S.K., Evans, J.S., Stevens, M.H., Ajello, J.M., Mayyasi, M.A., and Schneider, N.M. (2022), MAVEN/IUVS observations of C I 156.1 nm and 165.7 nm dayglow: Direct detection of carbon and implication on photochemical escape, Icarus, 371, 114664, https://doi.org/10.1016/j.icarus.2021.114664

López-Valverde, M.A., J.C. Gerard, F. González-Galindo, A.C. Vandaele, I. Thomas, O. Korablev, N. Ignatiev, A. Fedorova, F. Montmessin, A. Määttänen, S. Guilbon, F. Lefevre, M.R. Patel, S. Jiménez-Monferrer, M. García-Comas, A. Cardesin, C.F. Wilson, R.T. Clancy, A. Kleinböhl, D.J. McCleese, D.M. Kass, N.M. Schneider, M.S. Chaffin, J.J. López-Moreno, J. Rodríguez, Investigations of the Mars upper atmosphere with ExoMars trace gas orbiter. Space Sci. Rev. 214(1), 29 (2018). https://doi.org/10.1007/ s11214-017-0463-4

McClintock, W. E., Schneider, N. M., Holsclaw, G. M., Clarke, J. T., Hoskins, A. C., Stewart, I., et al. (2014). The Imaging Ultraviolet Septrograph (IUVS) for the MAVEN Mission. *Space Science Reviews*, *195*(1-4), 75–124. https://doi.org/10.1007/s11214-014-0098-7.

Simon, C., Witasse, O., Leblanc, F., Gronoff, G., & Bertaux, J. L. (2009). Dayglow on Mars: Kinetic modelling with SPICAM UV limb data. *Planetary and Space Science*, *57*(8-9), 1008-1021.

Stevens, M.H., J.S. Evans, N.M. Schneider, A.I.F. Stewart, J. Deighan, S.K. Jain, M. Crismani, A. Stiepen, M.S. Chaffin, W.E. McClintock, G.M. Holsclaw, F. Lefèvre, D.Y. Lo, J.T. Clarke, F. Montmessin, B.M. Jakosky, N2 in the upper atmosphere of Mars observed by IUVS on MAVEN. Geophys. Res. Lett. 42, 9050–9056 (2015). https://doi.org/10.1002/2015GL065319

Stevens, M. H., et al. (2017), Martian mesospheric cloud observations by IUVS on MAVEN: Thermal tides coupled to the upper atmosphere, Geophys. Res. Lett., 44, 4709–4715, doi:10.1002/ 2017GL072717.

Stewart, A.I., Mariner 6 and 7 ultraviolet spectrometer experiment: implication of CO+2 , CO, and O airglow. J. Geophys. Res. 77, 54–68 (1972). https://doi.org/10.1029/JA077i001p00054

Stewart, A. I. F., Alexander, M. J., Meier, R. R., Paxton, L. J., Bougher, S. W., & Fesen, C. G. (1992). Atomic oxygen in the Martian thermosphere. *Journal of Geophysical Research: Space Physics*, *97*(A1), 91-102.

Strickland, D. J., Thomas, G. E., & Sparks, P. R. (1972). Mariner 6 and 7 ultraviolet spectrometer experiment: Analysis of the OI 1304-and 1356-A emissions. *Journal of Geophysical Research*, *77*(22), 4052-4068.

Strickland, D. J., Stewart, A. I., Barth, C. A., Hord, C. W., & Lane, A. L. (1973). Mariner 9 ultraviolet spectrometer experiment: Mars atomic oxygen 1304-A emission. *Journal of Geophysical Research*, *78*(22), 4547-4559.

Wu, C. R., & Judge, D. L. (1979). The atomic oxygen 1304 Å emission produced through photodissociation of CO and CO2. *Chemical Physics Letters*, *68*(2-3), 495-498.

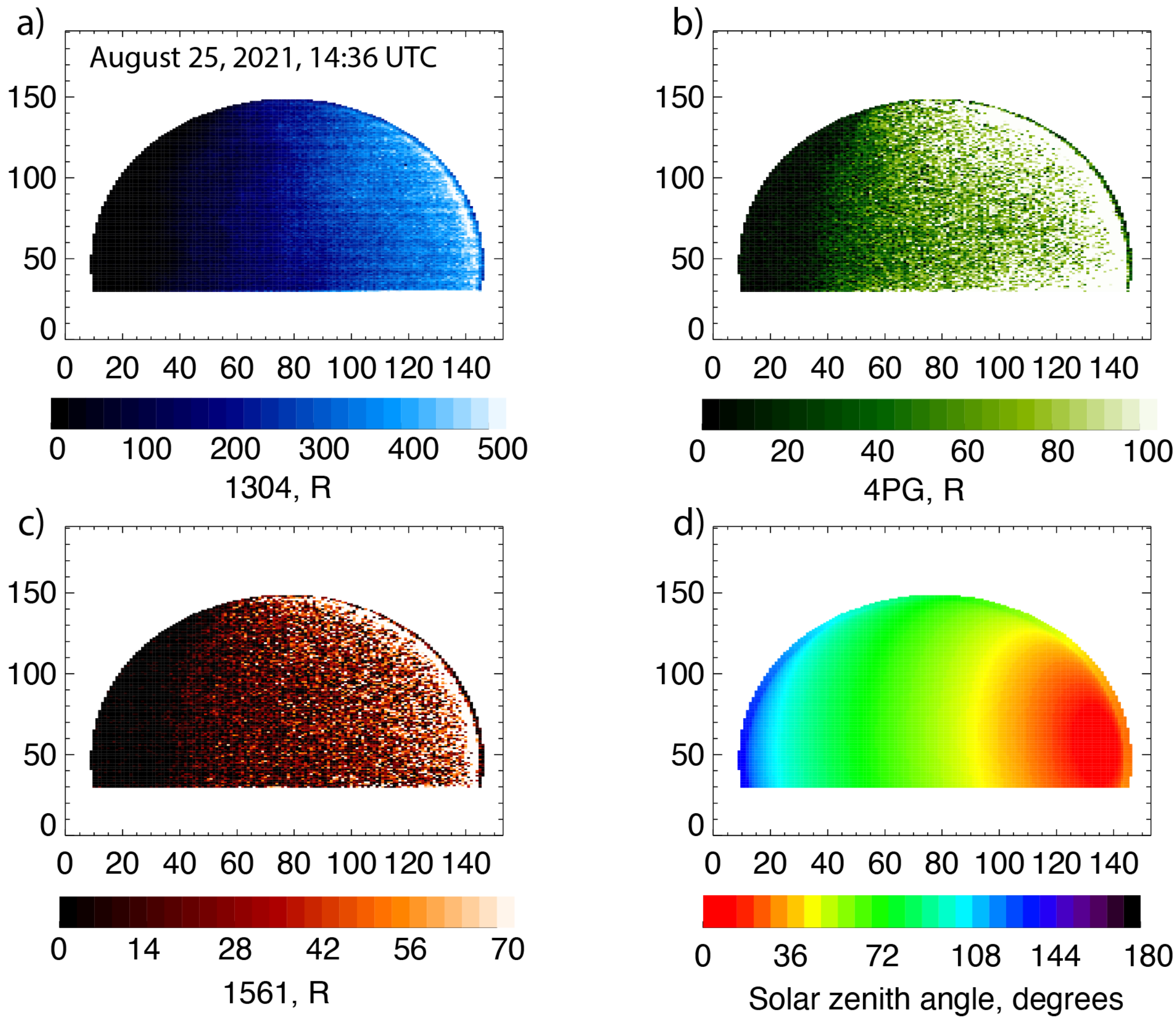

Figure 1 Example OS1 disk observation. Panels a through c show the brightness of O1304, CO4PG, and C1561, respectively. Panel d shows the solar zenith angle of each point on the disk. In each panel, the vertical dimension corresponds to the instantaneous imaging direction and the horizontal dimension corresponds to the motion of the imaging slit. The horizontal banding visible in O1304 results from imperfections in the instrument flatfield along the imaging direction.

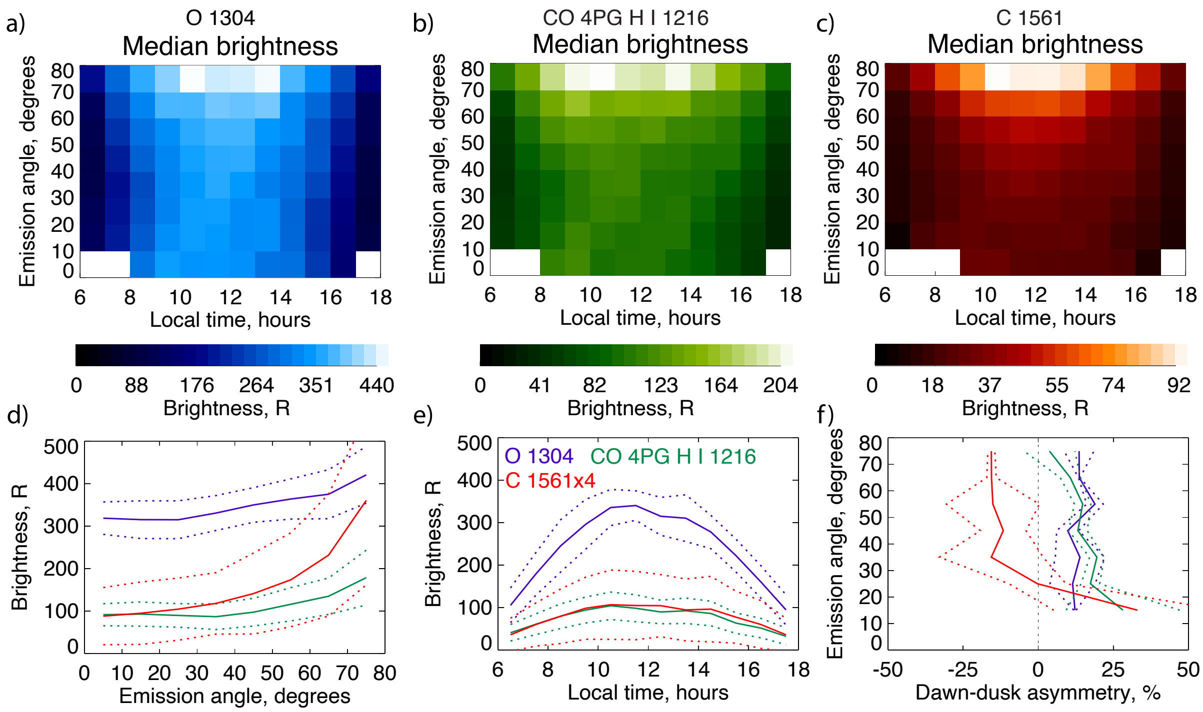

Figure 2 – Panels a through c show the brightness of the O1304, CO4PG, and C1561, respectively, as functions of LT and EMA. The median values of the emissions observed from ±5° of the equator, during June 11 – September 15, 2021, are shown. Panel d shows the variation in brightness at 12 – 13 hours LT with EMA, where the solid lines correspond to the median values and the dotted lines show the uncertainty corresponding to one standard deviation. Panel e is as panel d, but for the values from 20 – 30° EMA, as a function of LT. C1561 has been increased by a factor of 4 in panels d and e for clarity. Panel f shows the dawn-dusk asymmetry in the brightness of the emissions. Here, dawn corresponds to 7 – 8 hours LT, and dusk to 16-17 hours LT. The percent values correspond to (dawn-dusk)/dusk.

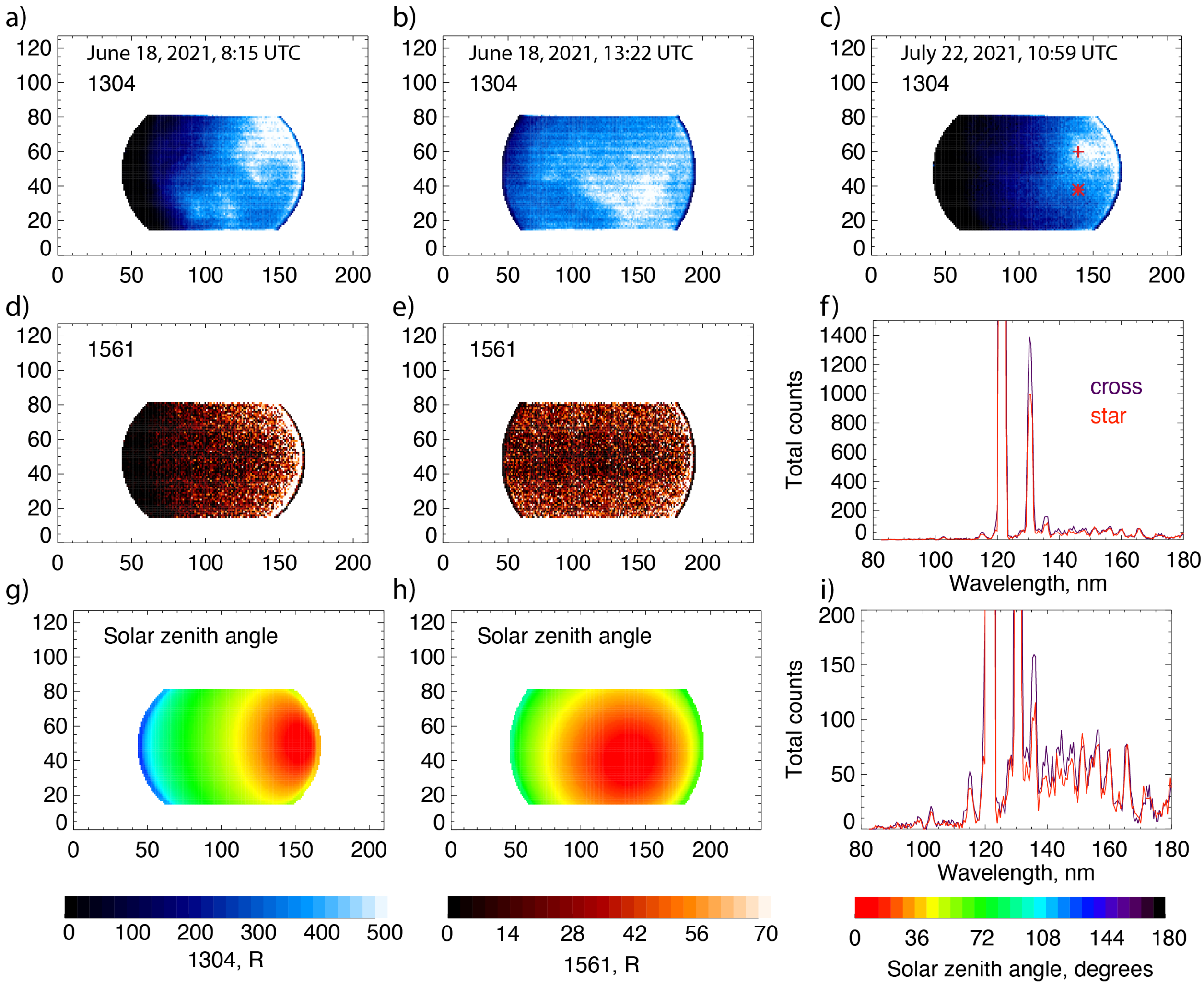

Figure 3 Examples of irregularly shaped dayglow variations. The left two columns correspond to a pair of observations on the same day. The brightness of O1304 and C1561 are shown, along with the corresponding SZA for each image. The irregularly shaped variations are clear in O1304 emission in both cases, and absent in C1561. Panel c shows another example of an irregularly shaped variation in O1304. The cross corresponds to a point at 26° SZA, 39° EMA, and the star is at 28° SZA, 38° EMA. The spectra shown in panels f and i correspond to sum of 9 pixels around the cross and star locations shown in panel c.

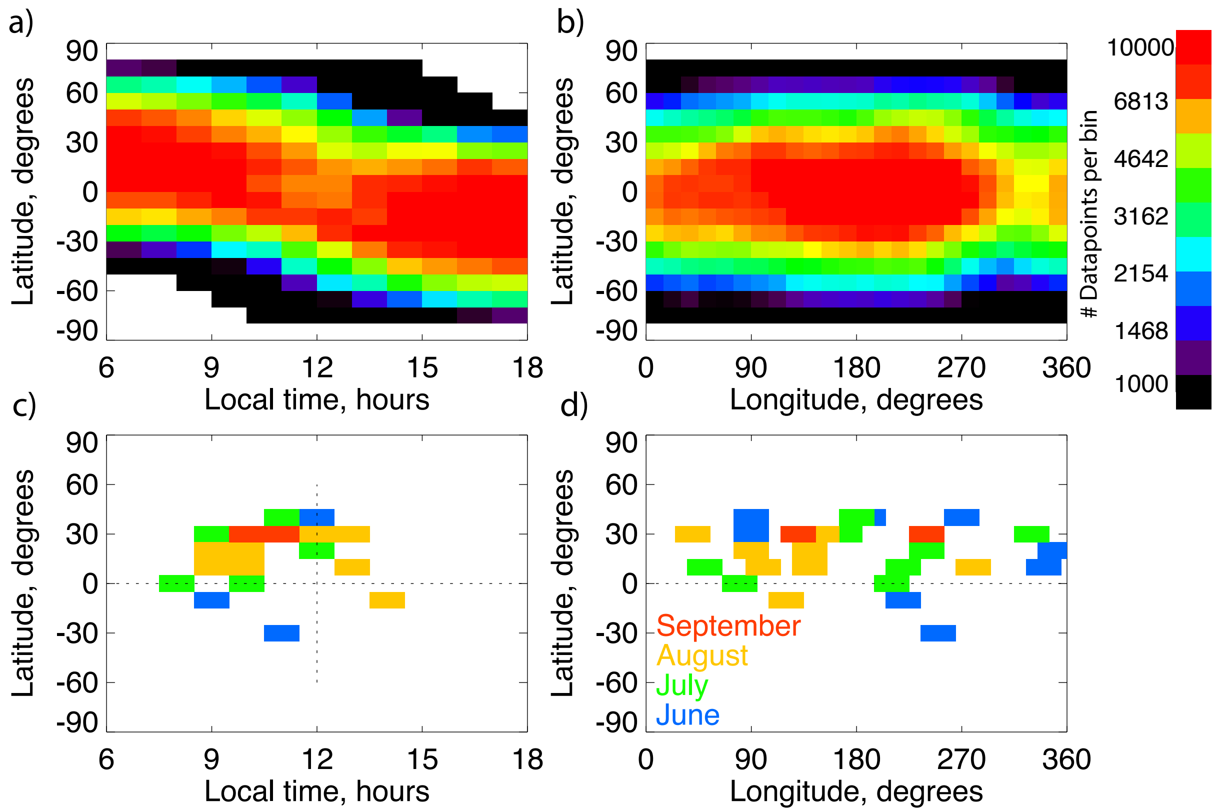

Figure 4 Distribution of the dayglow observations, and approximate locations of the irregularly shaped bright features seen in O1304. Panels a and b show the number of observations from June 11 – September 15, 2021, as functions of latitude and local time and latitude and longitude, respectively. Panels c and d show the approximate locations of the irregularly shaped bright features, as functions of latitude and longitude and latitude and local time, respectively. The color-coding corresponds to the month of the observation. Note that some locations overlap, such as near 9 – 11 hours LT, 10 – 30° north in panel d. A complete listing of the locations and dates is given in the Supplementary Data.